CHAPTER 5

Results and discussion (part II): Effect of Bi_2O_3 addition on properties BCZT ceramics and effect of PMNT single crystal on properties of BCZT-*x*Bi ceramics

In this chapter, the properties of Bi_2O_3-added BCZT ceramics and PMNT single crystal-added BCZT/Bi_2O_3 ceramics were demonstrated. The addition of low melting point (890°C [89]) Bi_2O_3 into BCZT ceramics was carried out to decrease the sintering temperature of the BCZT ceramics. The reduced sintering temperature resulted from Bi_2O_3 additions was observed for $BaTiO_3$ and BCZT ceramics [89, 90]. In the previous work [89], different amount of Bi_2O_3, i.e. 0.1, 0.5 and 1 mol%, was added into BCZT ceramics. They reported that the sintering temperature was reduced from 1500°C to 1300°C in which the BCZT powder was prepared by a conventional solid state method. The optimum amount of added-Bi_2O_3 was 0.1 mol% which much pronounced on the improvement of ceramics' properties. However, in this study, low amounts of Bi_2O_3 were added into BCZT powders prepared by a different synthesis method. The effects of Bi_2O_3, thereafter represented by Bi, additions on phase, microstructure, dielectric, ferroelectric properties of BCZT system where x = 0.005, 0.01, 0.02 and 0.1 mol% were investigated. In addition, the BCZT-Bi ceramics with an optimum Bi added content were selected to be the subjects to add PMNT single crystals to form BCZT-*x*Bi-*y*PMNT system where y = 1, 3 and 5 wt%. Finally, the relationship between the amount of the additives and their properties was discussed.

5.1 BCZT-*x*Bi powder characterizations

XRD patterns of BCZT-*x*Bi ceramics are shown in Fig. 5.1. For BCZT, BCZT-*0.005*Bi, BCZT-*0.010*Bi and BCZT-*0.020*Bi ceramics, the patterns showed that the materials possessed a pseudo-cubic perovskite phase without any impurity phase**.** A very slight peak shift to the right indicated a small lattice contraction with increasing Bi_2O_3 addition. It can be explained by substitution of Ba^{2+} (1.61 Å) or Ca^{2+} (1.34 Å) ions located on A-

site lattice by Bi^{3+} (1.03 Å) ions. This observed result was attributed to the shrinkage of the cell volume. On the other hand, the secondary phase of Bi_2O_3 (JCPDS no.10-761-730) was presented in the BCZT-*0.100*Bi ceramic. The phase of the ceramic also transformed into a tetragonal structure as implied from the observed peak splitting at 2θ ~ 45° and 66°. The observed unit cell contraction in this ceramic could be caused by the formed secondary phase, which created the point defects of Bi and O vacancies [91], as shown in Equation (5.1).

$$2Bi^{3+}+3O^{2-} \longrightarrow Bi_2O_3\uparrow +2V_{Bi}'''+ 3V_O^{\cdot\cdot} \qquad (5.1)$$

These results indicated that the dissolution and diffusion of Bi^{3+} into BCZT structure occurred and the solubility limit was between 0.02 and 0.1 mol% of Bi_2O_3.

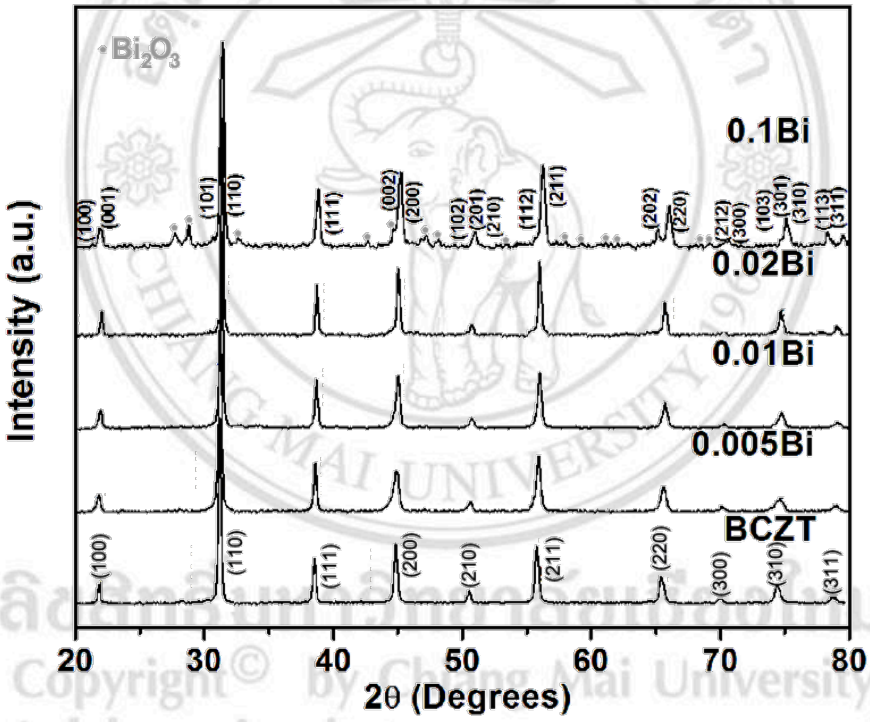

Figure 5.1 XRD patterns of BCZT-*x*Bi ceramics sintered at 1200°C.

5.2 Microstructures of BCZT-*x*Bi ceramics

SEM images of fractured surfaces of BCZT-*x*Bi ceramics are shown in Fig. 5.2. The monolithic BCZT ceramic consisted of small grains (< 1 μm) due to the nanometer-sized starting powder produced from the sol-gel auto-combustion method [19]. The presence of small pores indicated that the thermal energy from the sintering temperature of 1200°C was not enough to undergo a complete densification of the BCZT ceramic. The

morphology of BCZT-*0.005*Bi and BCZT-*0.0100*Bi ceramics showed a washed-out granular structure. This might be due to uneven distribution of Bi_2O_3 in these two samples which induced some low-melting compounds covering specific regions in the ceramics. Sporadically distributed large pores were also present in these samples which led to their low relative density values. For the BCZT-*0.020*Bi and BCZT-*0.100*Bi samples, the intergranular fracture and homogeneous grain size (~ 1 μm) distribution were observed. However, the relative density of BCZT-*0.020*Bi ceramic was much higher than that of BCZT-*0.100*Bi ceramic. This was thought to be due to partial evaporation of Bi_2O_3 [93, 94] and pore agglomeration into large voids of the latter, rendering its low observed density. Nevertheless, this study showed that addition of Bi_2O_3 in a suitable amount could improve the densification behavior and microstructure of BCZT ceramic [20, 95].

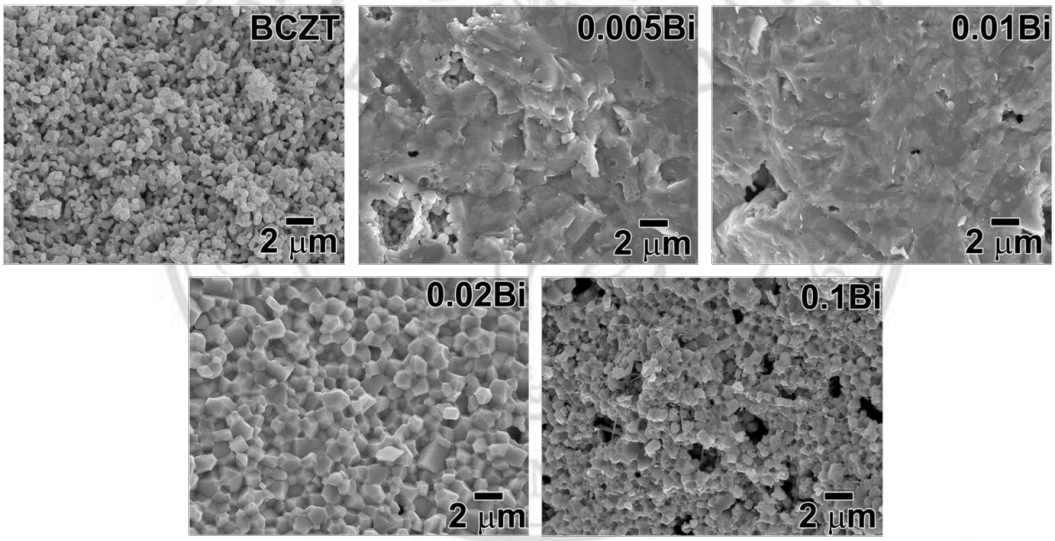

Figure 5.2 SEM micrographs of BCZT-*x*Bi ceramics sintered at 1200°C for 2 h.

The wavelength-dispersive spectroscopy (WDS) was used to analyze the optimized BCZT-*0.020*Bi ceramic using both point and area scanning modes as shown in Fig. 5.3-5.4. It suggested that the added-Bi_2O_3 diffused into the BCZT ceramic to form complete solid solution which confirmed the XRD result. Table 5.1 presents the atomic percentage from WDS analysis. The results showed that the BCZT-*0.020*Bi ceramic was consisted of Ba, Ca, Zr, Ti, O and Bi elements, confirming the expected composition of this ceramic.

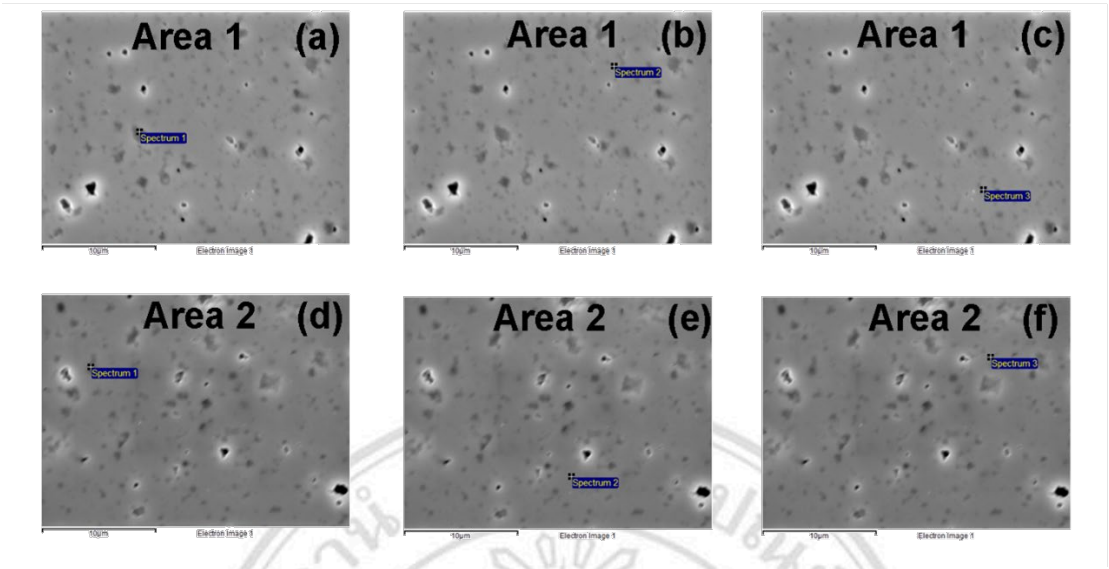

Figure 5.3 WDS point images of the BCZT-*0.020*Bi ceramic sintered at 1200°C for 2 h where area 1 (a) spectrum 1 (b) spectrum 2 (c) spectrum 3 and area 2 (d) spectrum 1 (e) spectrum 2 (f) spectrum 3.

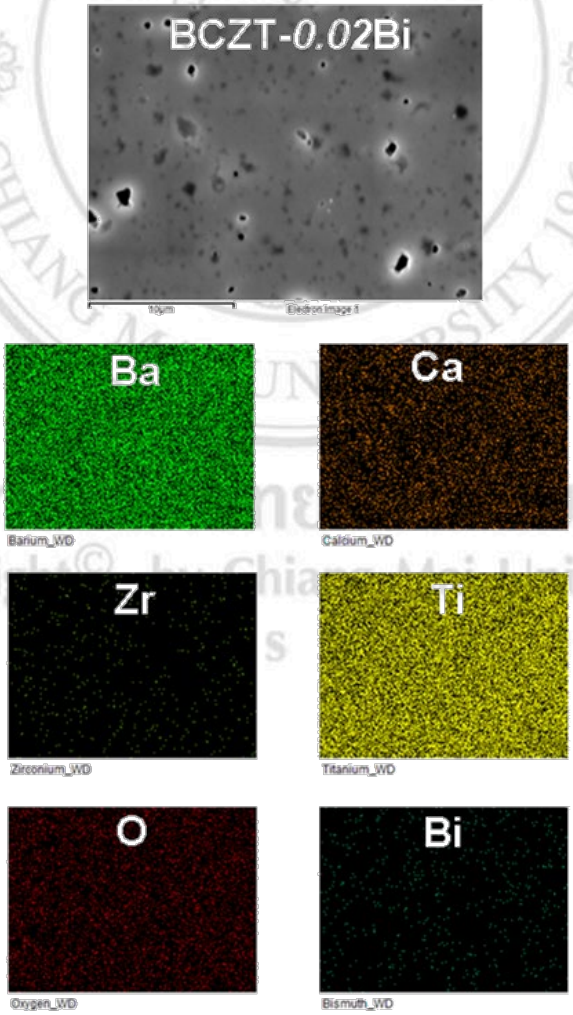

Figure 5.4 WDS mapping of the BCZT-*0.020*Bi sintered at 1200°C for 2 h.

Table 5.1 Chemical composition of selected the BCZT-*0.020*Bi ceramic sintered at 1200°C for 2 h.

Element / (Atomic%) Position analysis	Ba	Ca	Zr	Ti	O	Bi
Area 1 : spectrum1	24.563	5.224	1.284	27.204	39.936	1.789
Area 1 : spectrum2	24.473	3.711	2.185	24.876	43.947	0.807
Area 1 : spectrum3	21.508	4.631	1.926	24.756	46.64	0.54
Area 2 : spectrum1	23.891	3.989	1.951	24.678	44.4	1.091
Area 2 : spectrum2	23.436	4.338	1.695	24.72	45.154	0.657
Area 2 : spectrum3	24.61	3.97	1.763	24.801	44.025	0.832
Average atomic in sample (%)	0.84	0.15	0.06	0.90	1.53	0.03

5.3 Physical properties of BCZT-*x*Bi ceramics

Physical properties as a function of Bi_2O_3 content of BCZT-*x*Bi ceramics sintered at 1200°C for 2 h are shown in Fig. 5.5. A maximum relative density was observed for BCZT-*0.02*0Bi sample (~95%) while other compositions showed low relative densities (i.e. less than 90%) as black line and square symbol. This result indicated that addition of small amount of Bi_2O_3 could reduce the sintering temperature in BCZT to as low as 1200 °C compared to the typical sintering temperature of 1540°C [16, 80]. The BCZT-*0.020*Bi ceramic in this study also required lower sintering temperature than those employed in BCZT-*x*CuO [17], BCZT-*x*ZnO [92] and BCZT-*x*Bi_2O_3 (with higher Bi content than this work) [89] systems. The weight loss is shown as blue line. The values of the BCZT-*x*Bi ceramics tended to increase from 1.5 to 3% while the BCZT-*0.020*Bi sample exhibited the lowest ~1%. This was explained by the microstructural evolution as previously discussed. For shrinkage data, the BCZT-*x*Bi ceramics sintered at 1200°C for 2 h (red line), showed the values were in the range of 19-21%. The highest shrinkage of ~23% was observed in the BCZT-*0.020*Bi ceramic. Regarding Bi_2O_3 addition into the BCZT ceramic, the numerical results were not significantly different.

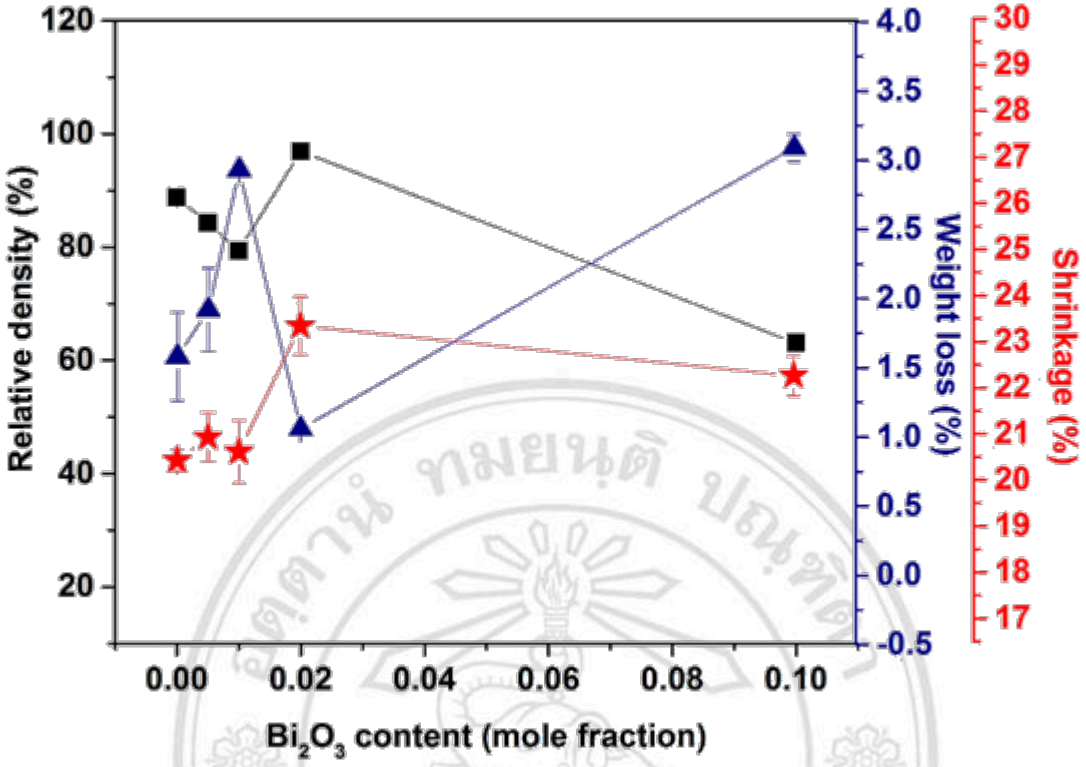

Figure 5.5 Physical properties as a function of Bi_2O_3 content of the BCZT-*x*Bi ceramics sintered at 1200°C for 2 h.

5.4 Dielectric properties of BCZT-*x*Bi ceramics

Plot of dielectric permittivity (ε_r) and dielectric loss (tan δ) at room temperature as a function of Bi_2O_3 content of BCZT-*x*Bi ceramics sintered at 1200°C for 2 h are shown in Fig. 5.6. The dielectric permittivity of the monolithic BCZT ceramic slightly increased with 0.005 and 0.010 mole fraction Bi_2O_3. It subsequently significantly increased with 0.020 mole fraction Bi_2O_3 addition. The results for BCZT-*0.1*Bi ceramic were not shown because it contained large pores and had low density. Value of tan δ decreased as Bi added content increased from 0.07 to 0.03 mole fraction. A lowest dielectric loss (~0.03) was obtained for the BCZT-*0.020*Bi ceramic because of the high sample's density and well-developed microstructure.

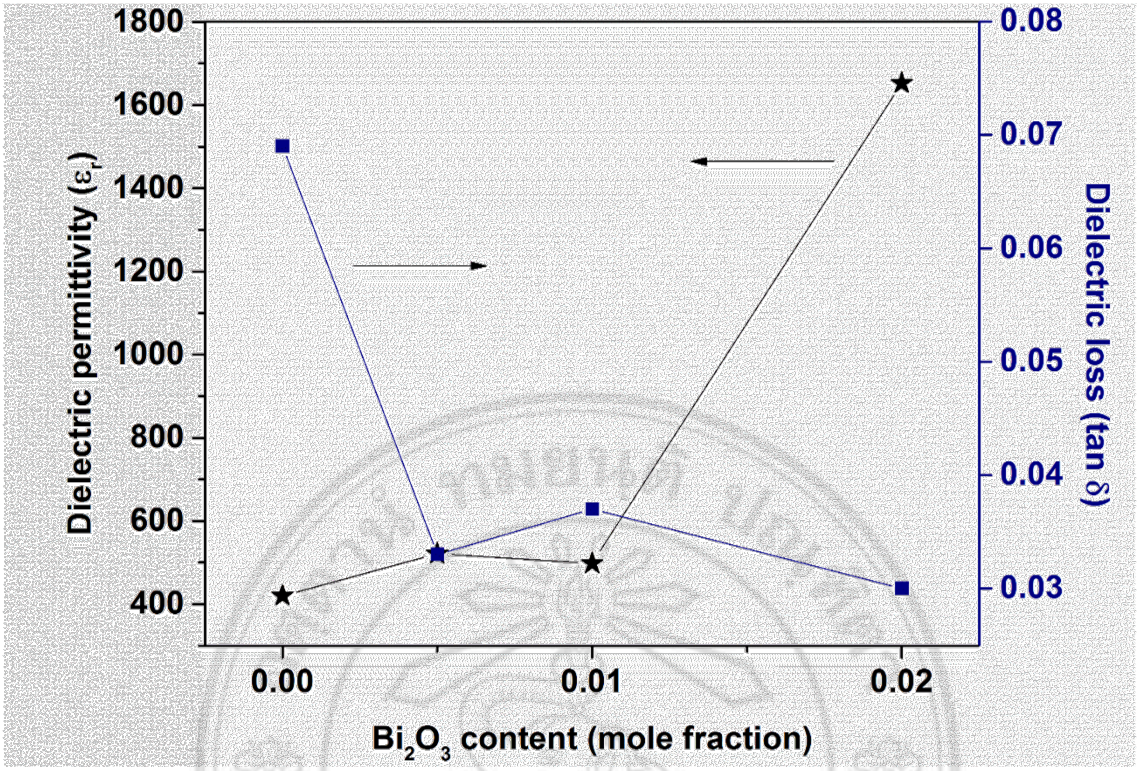

Figure 5.6 Plot of dielectric permittivity and dielectric loss as a function of Bi_2O_3 content of BCZT-*x*Bi ceramics sintered at 1200°C for 2 h.

5.5 Ferroelectric properties of BCZT-*x*Bi ceramics

Polarization-electric field (*P-E*) hysteresis curves are shown in Fig. 5.7. A monolithic BCZT ceramic presented a lossy loop due to its high porosity and possibly high conductive loss [96]. The presented porous could be the site at which charged defects are located. These charged defects could act as space charges that can be polarized under an applied field, resulting to the observed lossy *P-E* loop. The *P-E* curve became a slim loop with an addition of Bi_2O_3. This result seemed to agree with previous work which related the observed behavior to the presence of an ergodic relaxor state [53, 54, 97, 98]. For BCZT-Bi ceramics, *P-E* loop was slimmer when a higher Bi content was added. For BCZT-*0.100*Bi ceramic, due to its porous structure and large voids, its *P-E* curve could not be measured reliably. For BCZT-*0.020*Bi ceramic, a high maximum polarization (P_m ~6.0 μC/cm^2) was observed and the value reached ~7.5 μC/cm^2 when an electric field of 70 kV/cm was applied. This indicated a rather high electric field endurance of this sample.

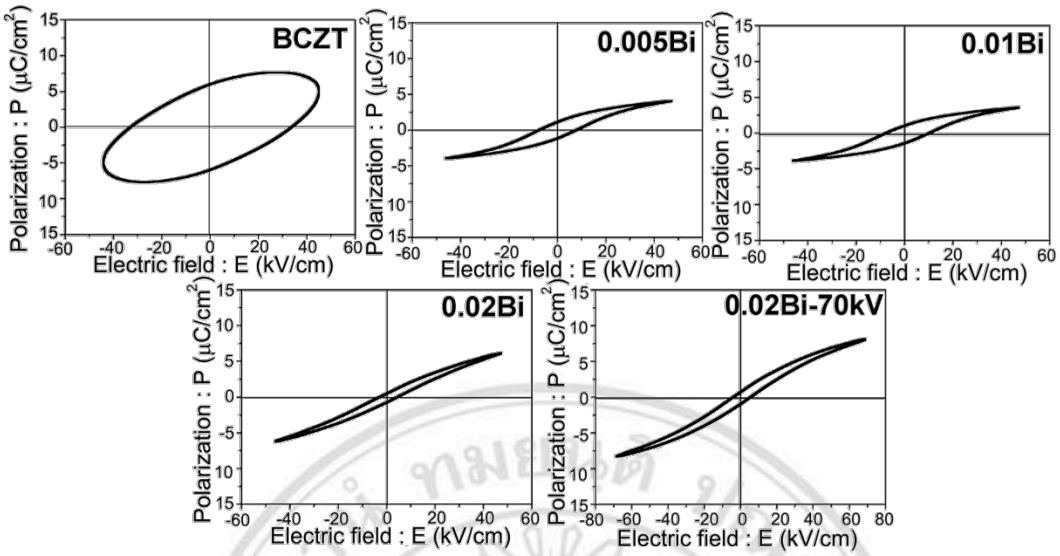

Figure 5.7 *P-E* hysteresis loops of BCZT-*x*Bi ceramics sintered at 1200°C for 2 h.

Since the optimum concentration of Bi_2O_3 addition in BCZT ceramic was 0.02 mole fraction thus this composition was used to produce ceramic composites. In this study PMNT single crystals were embedded into the BCZT-*0.020*Bi ceramic and sintered at 1200°C for 2 h. All samples were designed as BCZT-*0.02*Bi, 1PMNT, 3PMNT and 5PMNT ceramics (see in Chapter 3). The relationship between observed properties and PMNT crystal added content was discussed in details. The modified Curie-Weiss, Quadratic and Vogel-Fulcher laws were used to describe relaxor behavior of BCZT-*0.02*Bi-*x*PMNT ceramics.

5.6 Structure and crystal structure of BCZT-*0.02*Bi-*x*PMNT ceramics

Figure 5.8 illustrates XRD patterns of BCZT-*0.02*Bi (crushed), 1PMNT (pellet), 3PMNT (pellet), 5PMNT (pellet) ceramics and PMNT crystal. The XRD pattern of the BCZT-*0.02*Bi presented a pure perovskite phase. It was much different from Fig. 5.11 because this pattern was observed by crushed ceramics which confirmed that it had no prefer-orientation of each diffraction plane. All PMNT added ceramics showed a single phase of the perovskite structure without any impurity phase. The peak splitting at 2θ~43-45° was observed in all the ceramics which confirmed the existence of the tetragonal phase. However, the peak splitting was not observed in the PMNT crystal. The XRD pattern of

the PMNT crystal presented very high intensity peaks at $2\theta \sim 21.98°$ and 44.76°, which were caused by the preferred orientations of the PMNT single crystal.

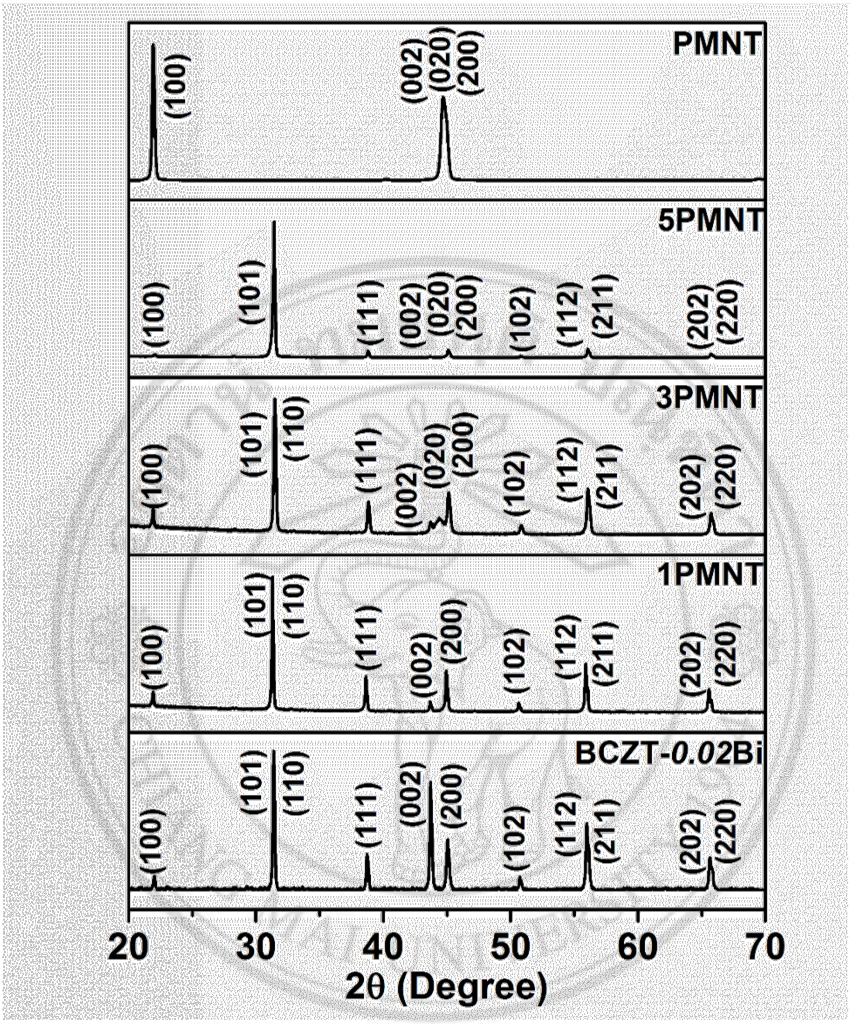

Figure 5.8 XRD patterns of BCZT-*0.02*Bi, 1PMNT, 3PMNT, 5PMNT ceramics and PMNT single crystal.

Normally, the rietveld refinement for the crystal structure uses for an analysis by the Powder Cell Software [61]. However, the PMNT crystal could not grind and crush to fine powder. Therefore, these results were observed and characterized from the pellets which were showed the preferred-orientations of each plans. Figure 5.9 shows the refinement results that were analyzed by Powder Cell Software of BCZT-*0.02*Bi, 1PMNT, 3PMNT and 5PMNT ceramics. The Rietveld refinement data of BCZT-*0.02*Bi and 1PMNT ceramics presented a tetragonal phase with P4mm space group. Nevertheless, the 3PMNT

and 5PMNT ceramics showed the existence of a rhombohedral symmetry with R3m space group and a tetragonal phase with P4mm space group. The fraction of the rhombohedral phase decreased from 25.9% for 3PMNT to 2.8% for 5PMNT ceramics while the fraction of tetragonal phase increased from 74.1% to 94.2% for 3PMNT and 5PMNT ceramics. For these results, the XRD patterns of 5PMNT showed the fraction of tetragonal phase which was lower than 3PMNT because it had the preferred-orientations of PMNT crystals and also showed the high intensity of XRD peaks. However, the cubic phase had used for refinement but it was not match. Therefore, the tetragonal and rhombohedral phases were selected to the fitting and the results showed very good fitting. Interface between the PMNT crystal and the BCZT-*0.02*Bi in small areas may be consisted of the rhombohedral phase but the tetragonal was mainly phase in the matrix. The observed results may be described by the different preferred-orientations of PMNT crystals in BCZT-*0.02*Bi ceramics. The lattice parameters of the ceramics were found to decrease with increasing PMNT crystal added content. The lattice parameters decreased from 4.0090 Å (a = b) for BCZT-*0.02*Bi to 4.0038 Å (a = b), 3.9908 Å (a = b) and 3.9838 and (a = b) for 1PMNT, 3PMNT and 5PMNT ceramics, respectively. Furthermore, the lattice parameter c of 4.0247 Å for BCZT-*0.02*Bi ceramic decreased to 4.0187 Å, 4.0081 Å and 4.005 Å for 1PMNT, 3PMNT and 5PMNT ceramics, respectively. This may be caused by the substitutions of smaller Pb^{2+} (1.19 Å) ions for Ba^{2+} ions (1.35 Å) while Nb^{5+} ions (0.64 Å) for Ti^{4+} ions (0.68 Å), leading to the unit cell contraction.

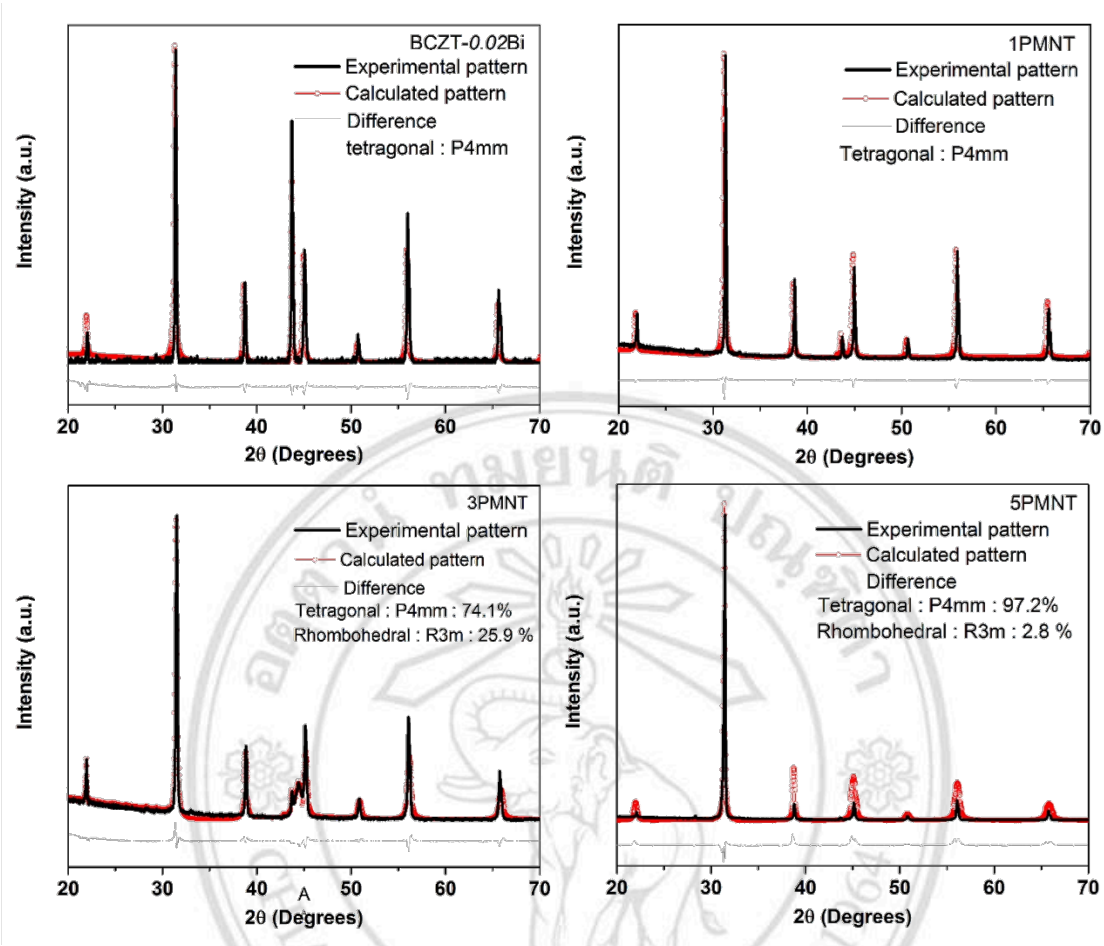

Figure 5.9 Fitting results of BCZT-0.02Bi, 1PMNT, 3PMNT and 5PMNT ceramics by Powder Cell Software.

5.7 Optical microscope image, microstructure and chemical composition of BCZT-*0.02*Bi-*x*PMNT ceramics

Figure 5.10 shows OM images of the BCZT-*0.02*Bi-*x*PMNT ceramic composites. It can be seen that embedded PMNT crystals showed different shapes such as triangle, rectangle and square (Fig. 5.10(a) - (c)). This was due to the orientation direction of the PMNT crystals embedded in the composites. This caused the difference in the side of crystals at which was polished, leaving those observed shapes, as schematically shown by the black areas in Fig. 5.10(d)-(e). Good mechanical bonding between PMNT crystals and BCZT-*0.02*Bi matrix was observed in the 1PMNT and 3PMNT composites, while the 5PMNT sample showed small cracks initially propagating from the interface between PMNT

crystal and BCZT-*0.02*Bi matrix, as shown in Fig. 5.10(c) and 5.11(c). This observed crack might be induced because the thermal expansion coefficient of PMNT ($10x10^{-6}$/°C) [11] is higher than BCZT ($6.17x10^{-6}$/°C) [12-13]. It should be noted that the extent of this white area, which was probably the diffusion zone, seemed to increase with increasing PMNT content.

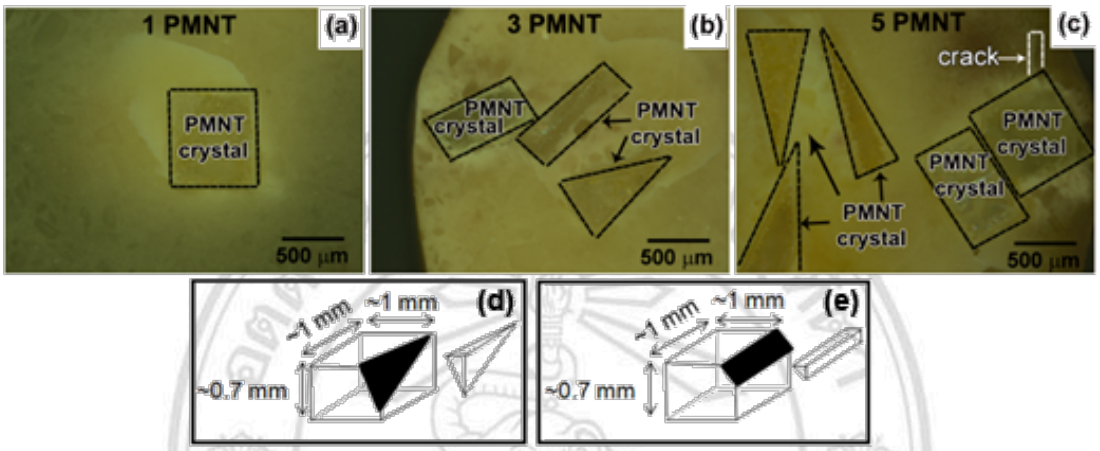

Figure 5.10 OM images of polished surfaces of the BCZT-*0.02*Bi-*x*PMNT composite ceramics: (a) 1PMNT, (b) 3PMNT, and (c) 5PMNT. Schematics of observed PMNT crystals with (a) triangle and (b) rectangle shapes due to polishing.

Figure 5.11 shows SEM images observed in the backscattered mode of polished surfaces of 1PMNT, 3PMNT and 5PMNT ceramics. The results area with different shades. It is generally known that, under the SEM backscattered mode, a material containing heavier atomic number elements presents a brighter shade as compared to a material with lower atomic number elements. In this case, the PMNT crystal has an average atomic number equal to 26.888 which was heavier than that of the BCZT-*0.02*Bi ceramic which has an average atomic number of 20.012. SEM images, energy dispersive X-ray (EDX) spectra and wavelength dispersive X-ray (WDS) spectra near the interface between the PMNT crystal and the BCZT-*0.02*Bi matrix of composites are shown in the Fig. 5.12 and Fig. 5.13. The light-gray area indicated by spectrum 1 in Fig. 5.12 contained high concentrations of Nb, Pb and Mg elements (21.12, 16.28 and 4.42 at%, respectively) which confirmed that this observed area belonged to a PMNT crystal. In contrast, the dark-gray area indicated by spectrum 2, no Pb was presented but it contained small

amounts of Nb and Mg (8.38 and 0.25 at%, respectively) elements. This result was consistent with the OM images that these elements could diffuse from a PMNT crystal into a BCZT-*0.02*Bi ceramic. The area of spectrum 2 also contained Ba, Ca, Zr and Bi and Ti elements, thus, it could be concluded that this area belonged to BCZT-*0.02*Bi.

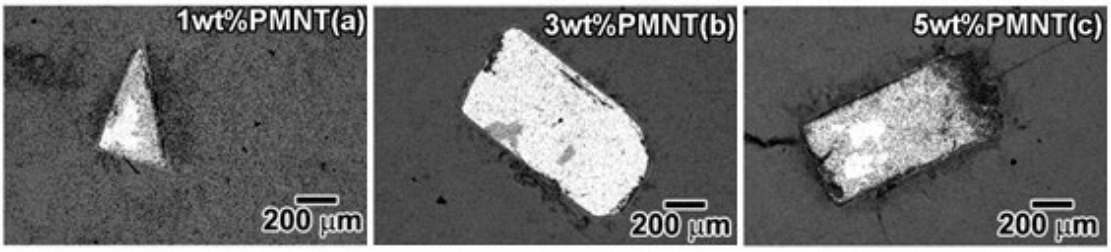

Figure 5.11 SEM images of the BCZT-*0.02*Bi-*x*PMNT composite ceramics of (a) 1PMNT (b) 3PMNT and (c) 5PMNT.

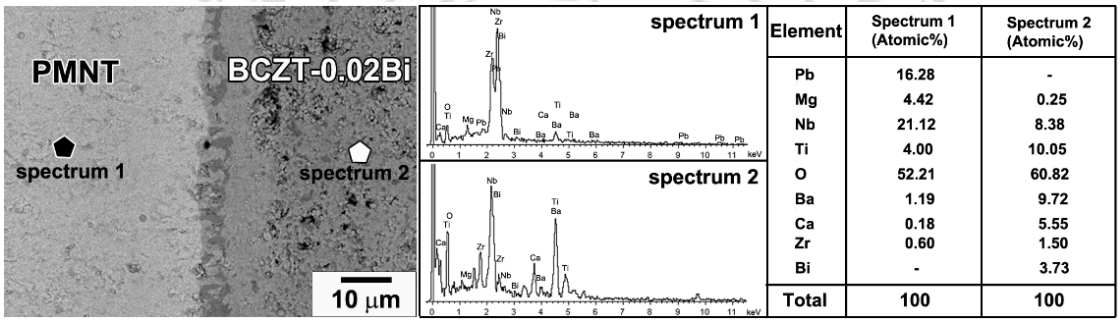

Element	Spectrum 1 (Atomic%)	Spectrum 2 (Atomic%)
Pb	16.28	-
Mg	4.42	0.25
Nb	21.12	8.38
Ti	4.00	10.05
O	52.21	60.82
Ba	1.19	9.72
Ca	0.18	5.55
Zr	0.60	1.50
Bi	-	3.73
Total	100	100

Figure 5.12 SEM image, EDX spectra and elemental analysis of the 3PMNT ceramic composite.

Figure 5.13 presents SEM images and WDS point analysis across PMNT-matrix interface. The PMNT area was also confirmed which showed the high contents of Pb, Nb and Mg elements while the BCZT-*0.02*Bi area presented of Ba, Ca and Zr elements. It was found that Nb and Mg elements diffused into the BCZT-*0.02*Bi area with the distance more than 10 μm from the original interface. This was due to they are smaller and lighter than Pb ion. However, Ba, Ca and Zr elements were observed the PMNT area with the distance only 10 μm from the original interface. Therefore, it could be assumed that the diffusion zone from the original interface was around 10 μm.

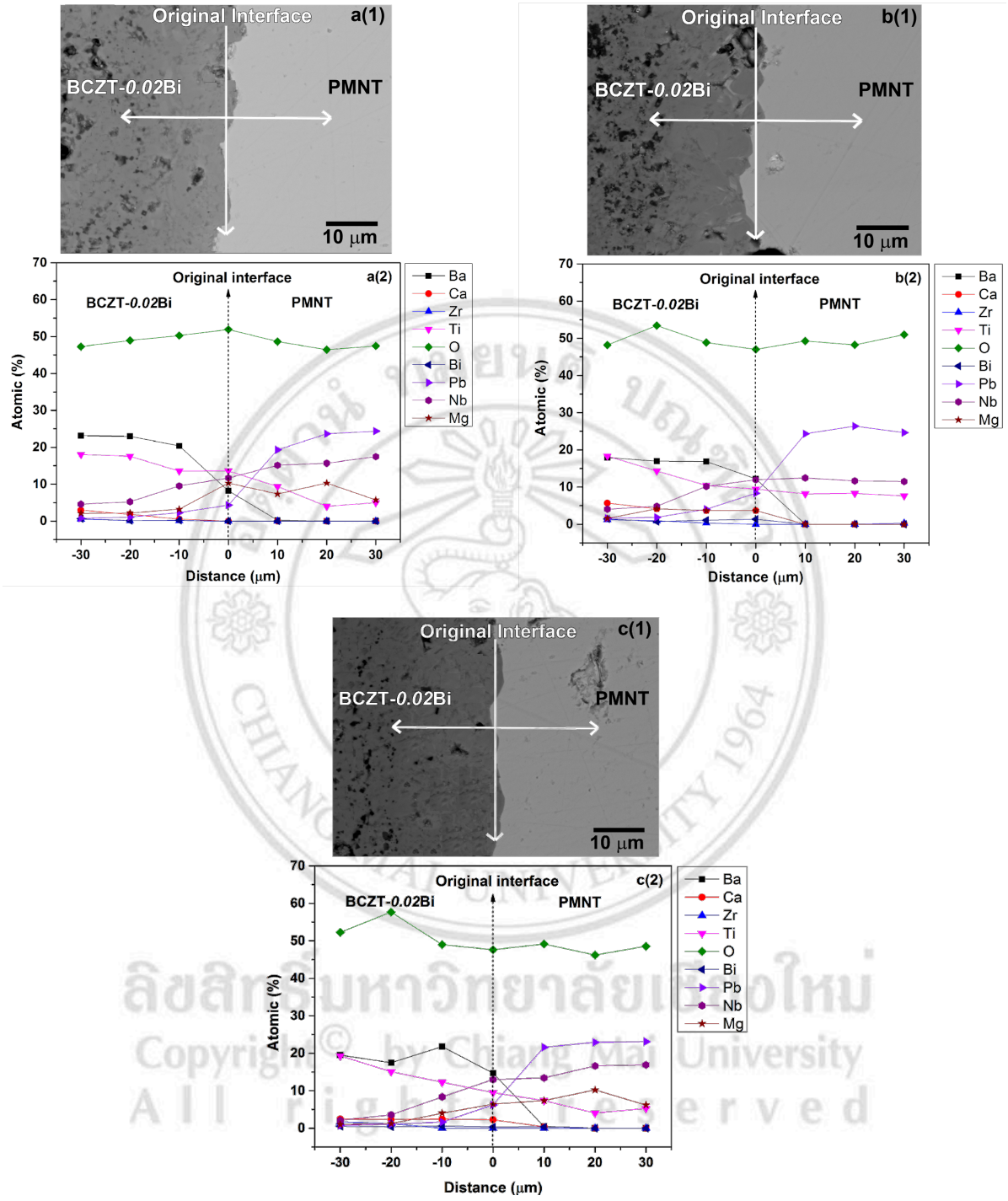

Figure 5.13 SEM images and elemental analysis by WDS for 1PMNT, 3PMNT and 5PMNT composites.

5.8 Dielectric properties of BCZT-*0.02*Bi-*x*PMNT ceramics

Figure 5.14 shows the variation of the dielectric permittivity (ε_r) and loss tangent ($\tan\delta$) of BCZT-*0.02*Bi-*x*PMNT composite ceramics as a function of temperature and frequency.

All samples showed the relaxor behavior which could be characterized by the broad dielectric permittivity maximum whose associated temperature (T_m) increased with increasing frequency. The values of ε_r (at 1 kHz) at room temperature were approximately 1690, 2417, 2582 and 2828 and the values of tan δ were 0.03, 0.004, 0.008 and 0.009, for BCZT-*0.02*Bi, 1PMNT, 3PMNT and 5PMNT, respectively. It should be noted that these room temperature values of ε_r and tan δ at 1 kHz were comparable or better than those of $BaTiO_3$ (1429, 0.004) and PZT (813, 0.011) ceramics [5]. All samples studied here could be categorized as a "canonical relaxor" because ε_r showed a smooth decrease in value at temperatures below T_m with no distinct or sharp transition point that could indicate a transition from the ergodic (ER) relaxor state to a ferroelectric (FE) phase [1]. The values of T_m and ε_r increased with increasing PMNT crystal content, which indicated that the PMNT crystals affected the nature of phase transformation in BCZT-*0.02*Bi ceramic. In this case, the random elastic fields and electric fields might be produced by the presence of PMNT, leading to the observed enhancement in relaxor behavior [15]. Additionally, the diffuse phase transition (DPT) temperatures at 100 kHz of all the samples were fitted and found to be in the range of typical relaxor behavior, with the γ–value close to 2 [16]: γ = 1.81 for BCZT-*0.02*Bi ceramic, 1.77 for 1PMNT, 1.82 for 3PMNT, 1.86 for 5PMNT and 1.97 for PMNT single crystals. Figure 5.15 shows the dielectric properties of BCZT-*0.02*Bi-*x*PMNT ceramic composites at different concentrations of PMNT crystals at 1 kHz. The dielectric constant (ε_r) at room temperature increased with the increasing amount of PMNT crystals. The low dielectric loss (tanδ) values in the PMNT-added samples indicated a near-zero loss and this behavior seemed to be in contrast with typical high-dielectric materials. The value of T_m exhibited an increasing trend, i.e. -56°C, -38 °C, -32°C and -10°C for BCZT-*0.02*Bi, 1PMNT, 3PMNT and 5PMNT ceramics, respectively. The reason for such a T_m variation was partly due to the fact that the PMNT crystal have higher T_m (~120°C) than the BCZT-*0.02*Bi ceramics (-56°C), as indicated in Figure 3. The maximum dielectric constant (ε_{max}) values slightly increased with increasing PMNT crystal content and were in the range of 2137-3016.

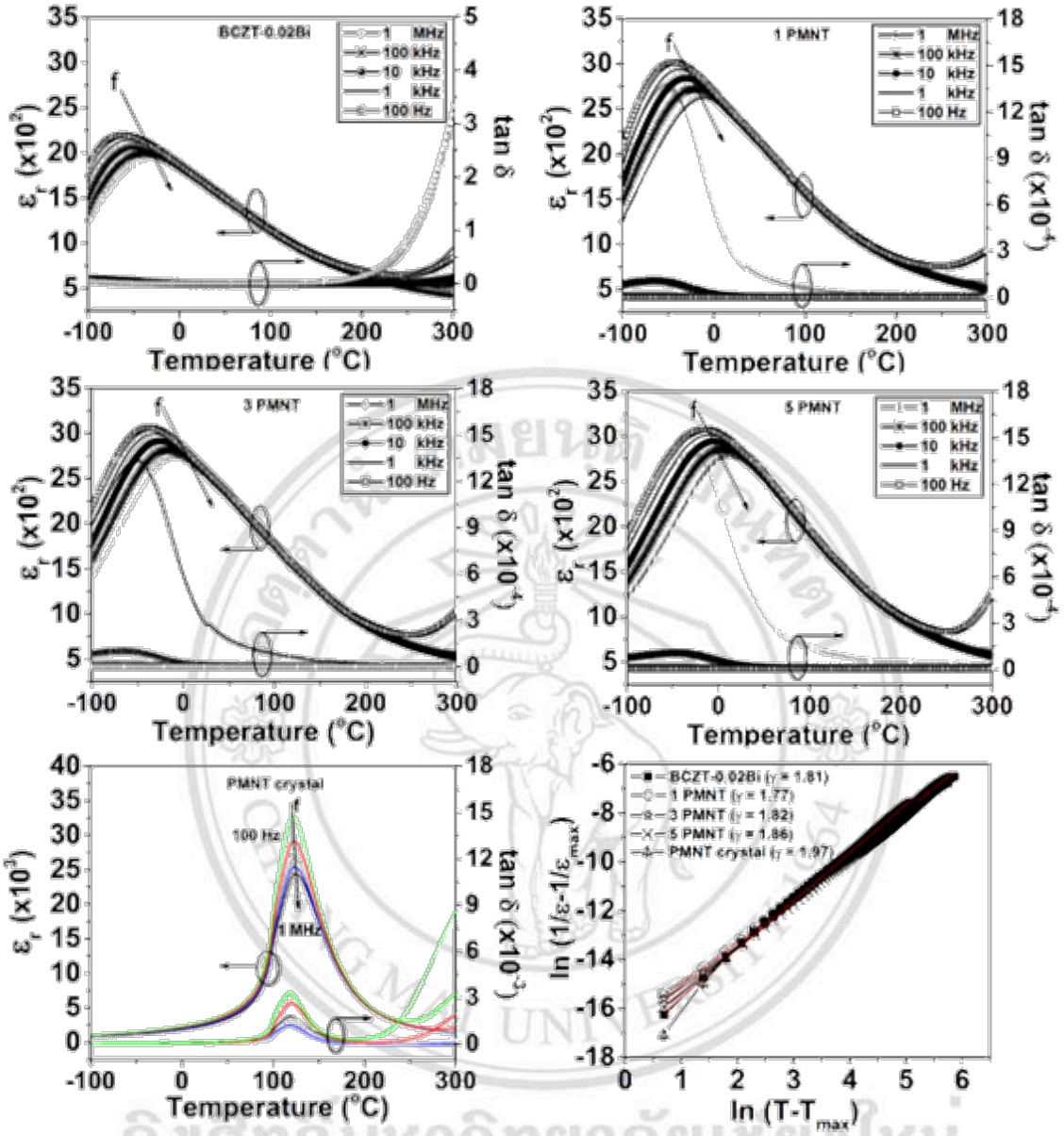

Figure 5.14 Temperature dependences of the dielectric permittivity (ε_r) and dielectric loss (tanδ) of BCZT-*0.02*Bi-*x*PMNT when x = 0, 1, 3 and 5 wt% PMNT single crystals (a - d), and those of a PMNT crystal (e). Fitting results of the broad dielectric peaks at 1 kHz.

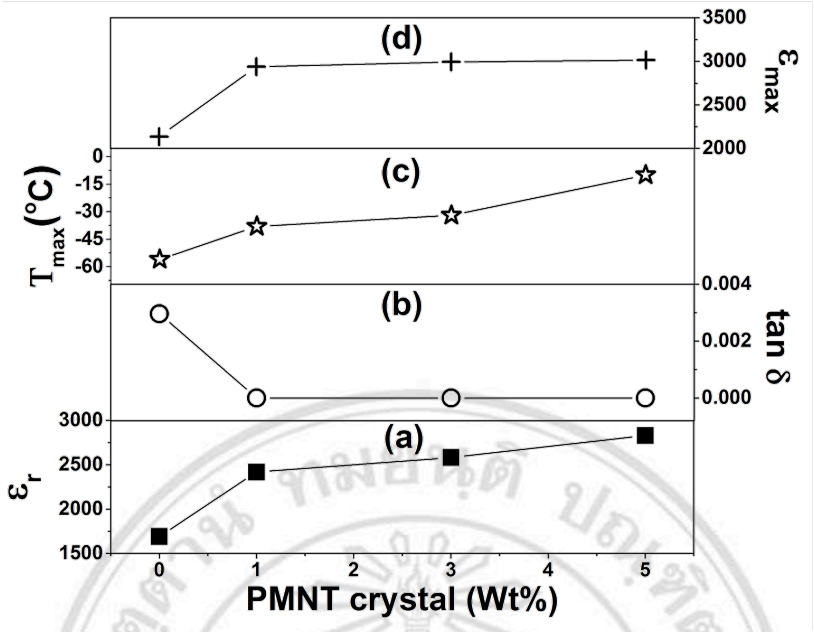

Figure 5.15 Dielectric properties of the BCZT-*0.02*Bi-*x*PMNT composite ceramics with different concentrations of PMNT crystals measured at 1 kHz.

5.9 Relaxor ferroelectric properties

The high temperature slope of permittivity peak can be characterized by equation 2.8. Figure 5.16 presents the modified Curie-Weiss law for the BCZT-*0.02*Bi-*x*PMNT composite ceramics and PMNT crystal. The results showed that T_{CW} increased with increasing PMNT crystals from 5.95°C, 42.57°C, 53.67°C, 65.42°C and 181.80°C for the BCZT-*0.02*Bi, 1PMNT, 3PMNT, 5PMNT and PMNT. The Curie constant values were term of 1.266 x 10^5 K, 1.316 x 10^5 K, 1.278 x 10^5 K, 1.328 x 10^5 K and 1.648 x 10^5 K which were good agreement with the same order of magnitude (~10^5 K) in relaxor materials. The T_{max} increased with PMNT content because the PMNT crystal (124°C) has higher T_{max} than the BCZT-*0.02*Bi ceramic (-38°C) as shown in Fig 5.14 and Table 5.2. T_B also increased with the addition of PMNT crystal which followed the trend of T_{max}. It might be concluded that the nucleation dynamic of PNRs increased with increasing PMNT crystal which was consisted of high number of PNRs in which Mg^{2+} and Nb^{5+} ions are fully or partially disordered in the B-sublattice of the ABO_3 perovskite structure [38].

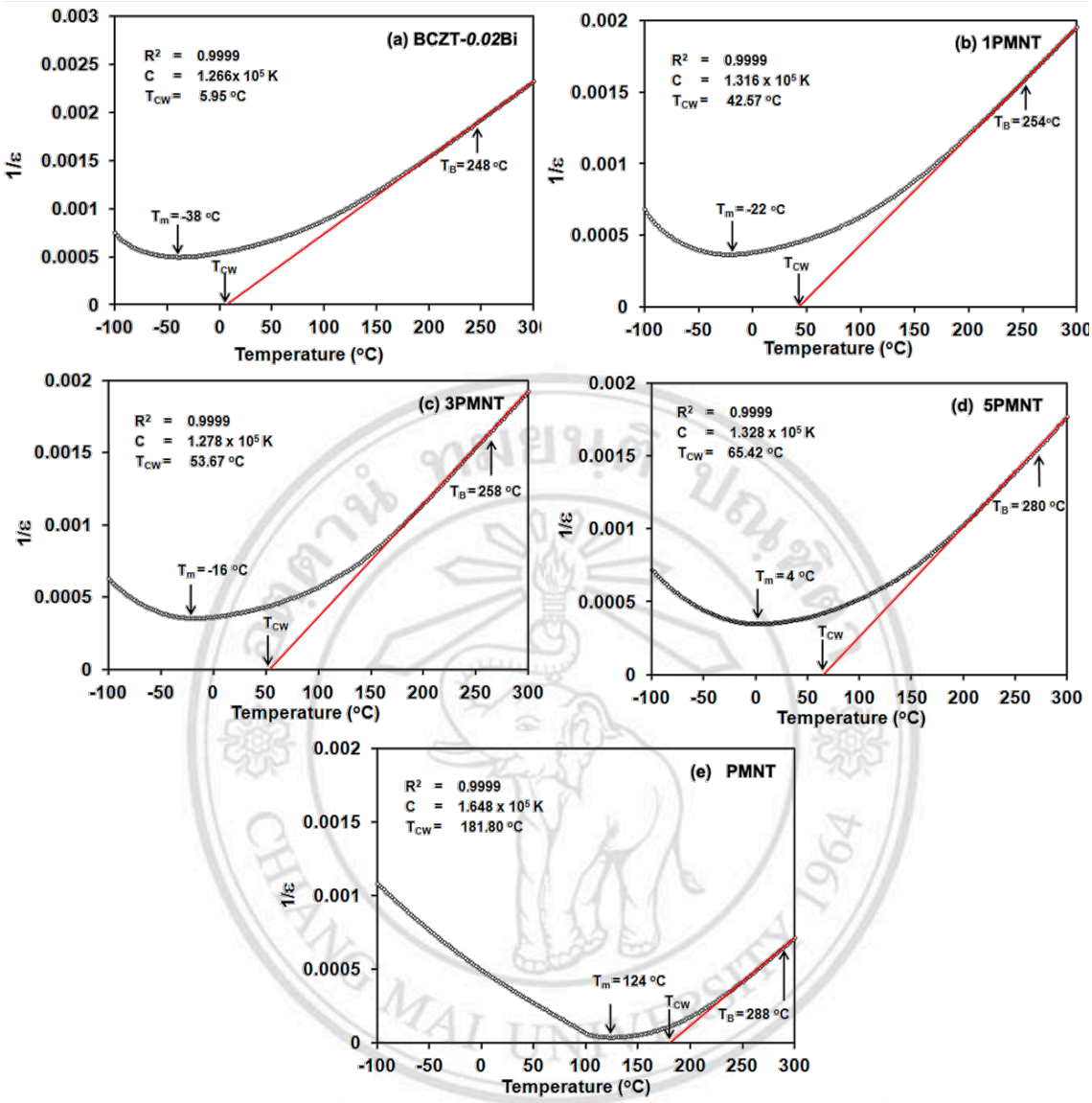

Figure 5.16 The modified of Curie-Weiss law for the BCZT-*0.02*Bi-*x*PMNT composite ceramics and PMNT crystal.

Table 5.2 Curie-Weiss parameters of the BCZT-*0.02*Bi-*x*PMNT composite ceramics.

PMNT content (wt%)	T_{CW} (°C)	T_m (°C)	T_B (°C)
0	5.95	-38	248
1	42.57	-22	254
3	53.67	-16	258
5	65.42	4	280
100	181.80	124	288

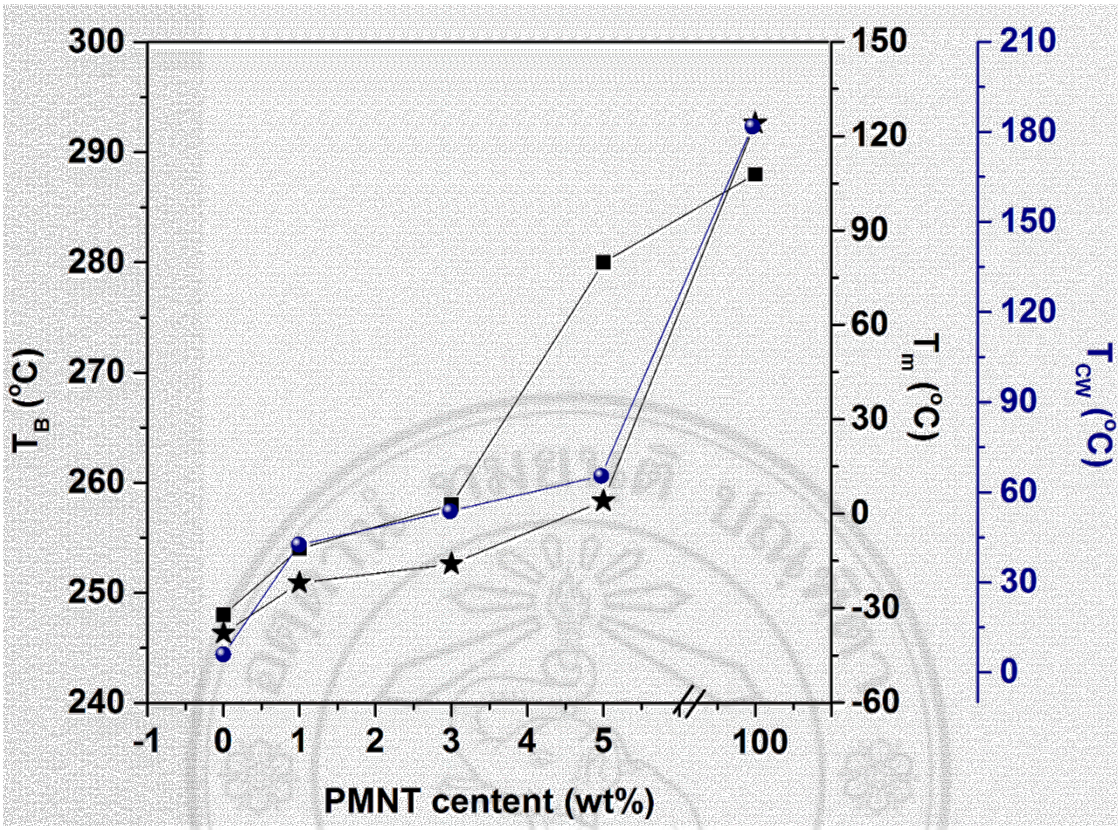

Figure 5.17 Plots of T_B, T_m and T_{CW} as a function of PMNT content of the BCZT-*0.02*Bi-*x*PMNT composite ceramics.

A relaxor ferroelectric behavior was also analyzed using the Quadratic law (equation 2.7) as mentioned in chapter 2. Figure 5.18 shows the fitting of the dielectric properties as a function of temperature for the BCZT-*0.02*Bi-*x*PMNT composite ceramics to the quadratic law using least square method. Very good fitting for all ceramics was obtained with the delta parameter (δ) approximately values of 189.45 ± 5.06 K, 163.95 ± 2.72 K, 148.13 ± 5.78 K, 136.99 ± 6.29 K and 29.19 ± 0.27 K for the BCZT-*0.02*Bi, 1PMNT, 3PMNT, 5PMNT ceramics and PMNT crystal, respectively. The measurement of the width of the permittivity peaks and diffuseness of permittivity peak was obtained as the δ. The sharper permittivity presented the smaller value of δ [64.]. Furthermore, this sharpening also showed as an increase in the maximum of dielectric constant as can be seen in Figure 5.18 which was in good agreement with previous report [64]. In this case, the trend of sharper peak increased with increasing the PMNT crystal which was thought to be related to the increasing size and number of the PNRs at a higher temperature.

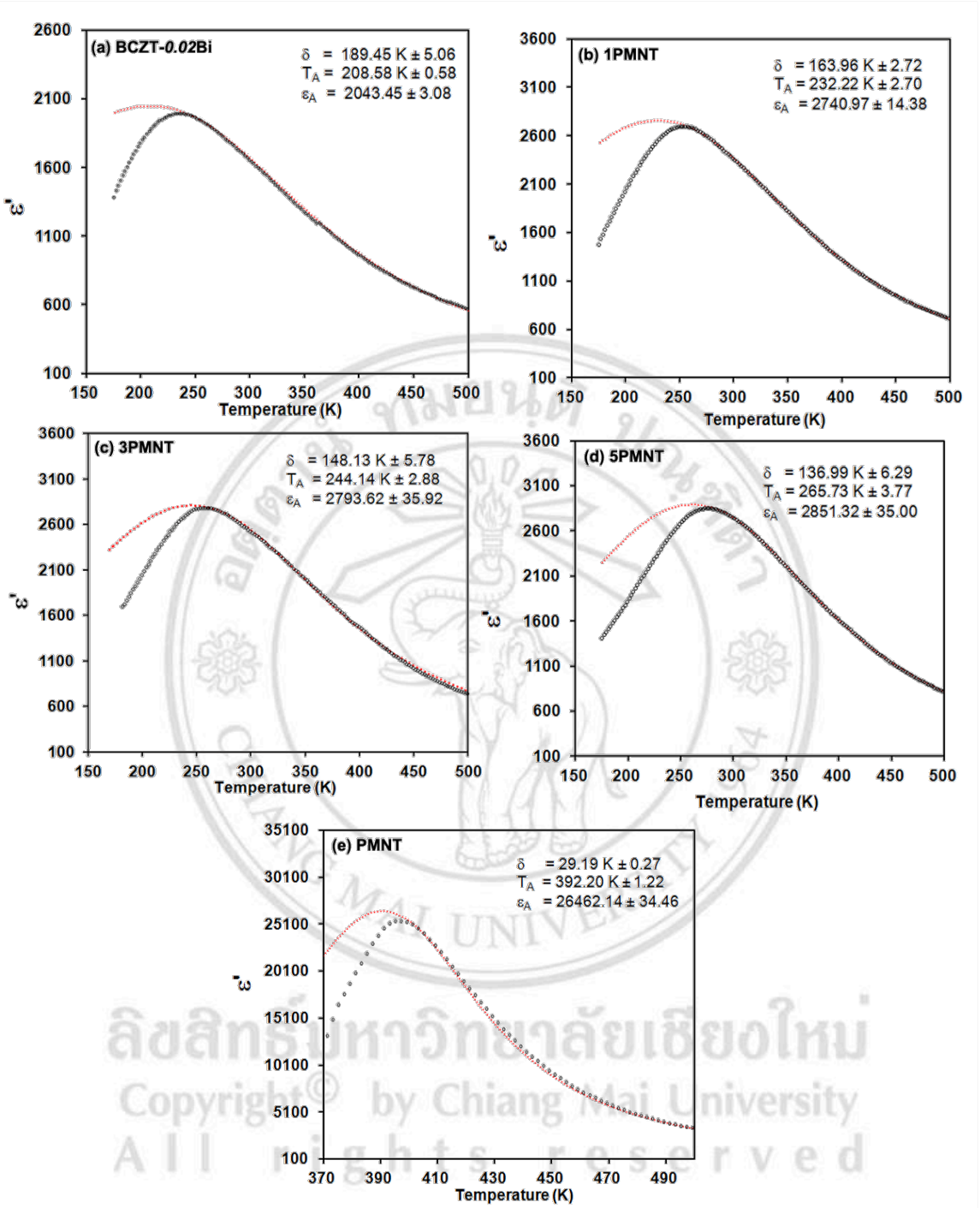

Figure 5.18 Quadratic fitting curves of (a) BCZT-*0.02*Bi and the ceramics added with (b) 1PMNT (c) 3PMNT (d) 5PMNT of the BCZT-*0.02*Bi-*x*PMNT composite ceramics and (e) PMNT crystal. Dot-black line and dot-red curves are belonged to an experimental data and the data investigated from a quadratic equation, respectively.

The fitting parameters are given in Table 5.3 and also plotted as a function of PMNT content as show in Figure 5.19. The change of the both static conventional permittivity (ε_A) and its temperature (T_A) were found to increase with increasing the PMNT crystal. The ε_A value increased from 2043.45 ± 3.08, 2740.97 ± 14.38, 2793 ± 35.92, 2851.23 ± 3.77 and 2646.14 ± 34.46 and T_A from 208.58 ± 0.58K, 232.22 ± 2.70, 244.14 ± 2.88, 265.73 ± 3.77, 392.20 ± 0.27. Another reason for this observed behavior may be increased in concentration of Ti^{4+} ions by addition of PMNT crystal into the BCZT-*0.02*Bi-*x*PMNT ceramics which has the long-range polar order and ferroelectrically active [64].

Table 5.3 Quadratic fitting parameters of the BCZT-*0.02*Bi-*x*PMNT ceramics.

PMNT content (wt%)	**T_A (K)**	**ε_A**	**δ (K)**
0	208.58 ± 0.58	2043.45 ± 3.08	189.45 ± 5.06
1	232.22 ± 2.70	2740.97 ± 14.38	163.95 ± 2.72
3	244.14 ± 2.88	2793 ± 35.92	148.13 ± 5.78
5	265.73 ± 3.77	2851.23 ± 3.77	136.99 ± 6.29
100	392.20 ± 0.27	2646.14 ± 34.46	29.19 ± 0.27

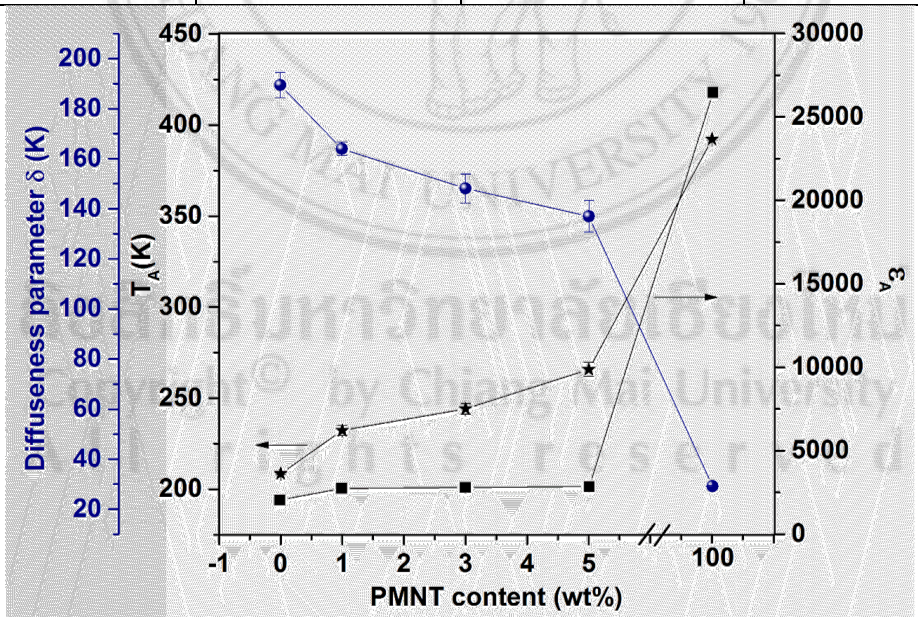

Figure 5.19 Plots of fitting parameters of ε_A, T_A and diffuseness parameters of the BCZT-*0.02*Bi-*x*PMNT composite ceramics as a function of PMNT content of PMNT content.

In order to study an effect of PMNT addition into BCZT-*0.02*Bi-*x*PMNT composite ceramics on a dynamic of dielectric relaxation, a dependence of frequency of T_{max} was fitted to a V-F law fitting curves of BCZT-*0.02*Bi-*x*PMNT composite ceramics shown in Figure 5.20. The experimental data were fitted well (solid-black line). All parameters such as T_{VF}, E_a and f_0 are given in Table 5.4 and Figure 5.21. The T_{VF} increased with increasing PMNT crystal fraction. The value of f_0 also increased which corresponded well with T_{max}. However, E_a decreased with increasing PMNT crystal from 0.1643, 0.1363, 0.1308, 0.1244 and 0.028 eV, respectively which it may be consumed lower activation energy of PNRs reorientation than BCZT-*0.02*Bi ceramics.

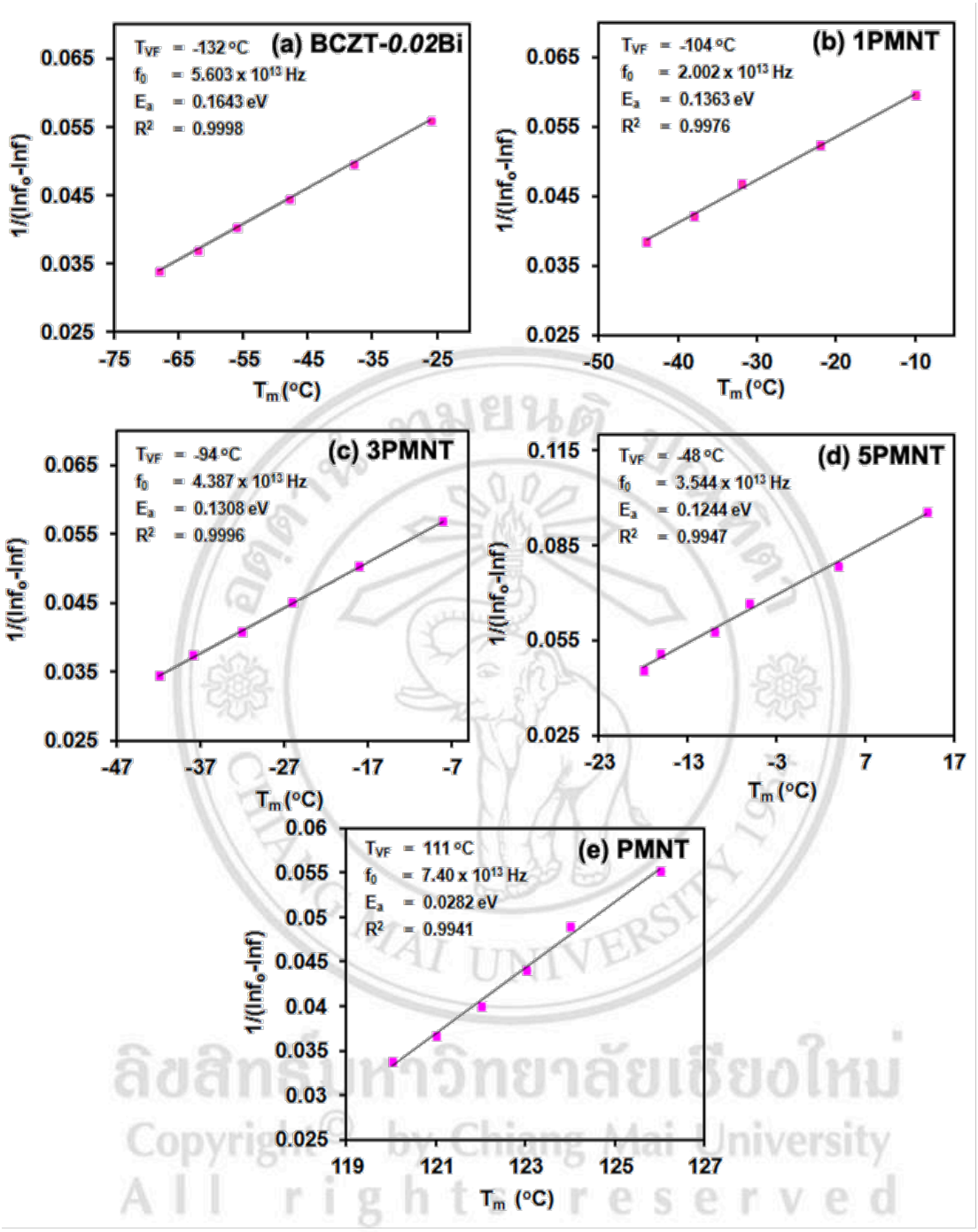

Figure 5.20 *V-F* fitting curves of (a) BCZT-*0.02*Bi ceramic and the ceramics added with (b) 1PMNT (c) 3PMNT (d) 5PMNT of the BCZT-*0.02*Bi-*x*PMNT composite ceramics and (e) PMNT crystal. Dot-pink line and solid-black curves are belonged to an experimental data and the data investigated from *V-F* equation, respectively.

Table 5.4 V-F fitting parameters of the BCZT-*0.02*Bi-*x*PMNT composite ceramics.

PMNT content (wt%)	T_{VF} **(°C)**	f_0 **(Hz)**	E_a **(eV)**
0	-132	5.603×10^{13}	0.1643
1	-104	2.002×10^{13}	0.1363
3	-94	4.387×10^{13}	0.1308
5	-48	3.554×10^{13}	0.1244
100	111	7.400×10^{13}	0.0282

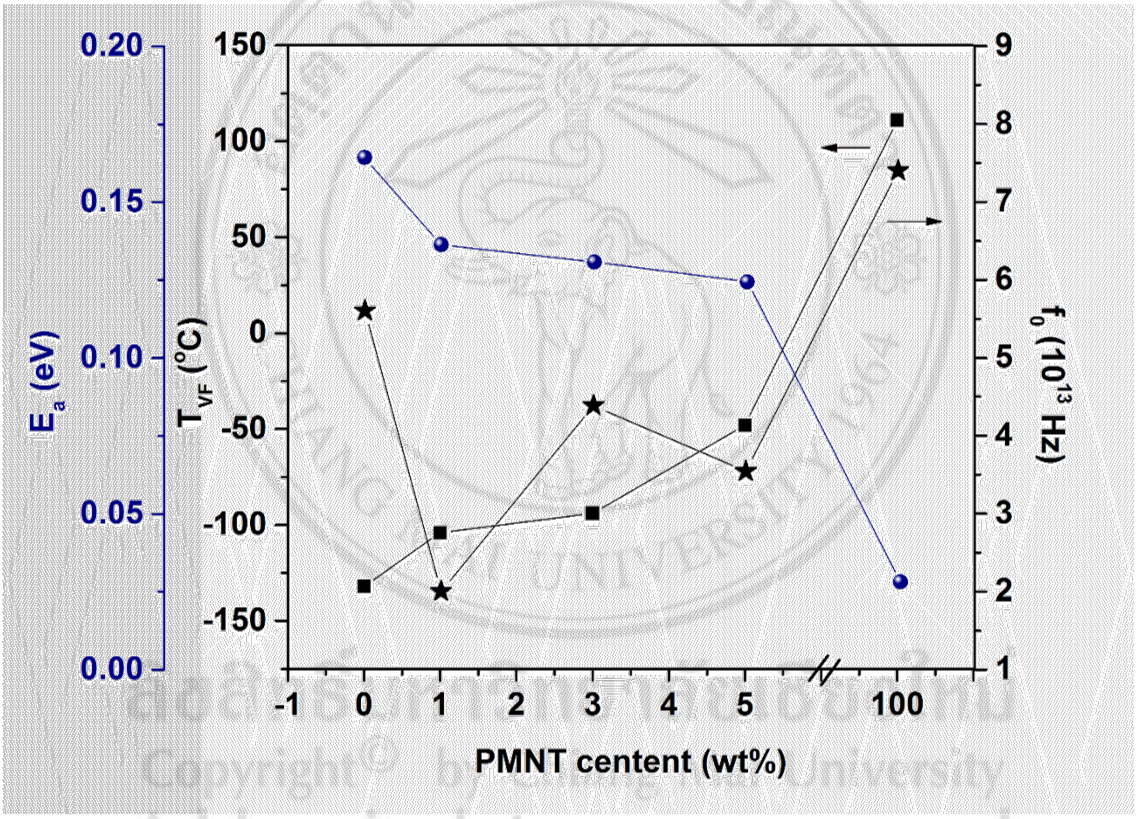

Figure 5.21 Plots of fitting parameters of E_a, f_0 and T_{VF} of the BCZT-*0.02*Bi-*x*PMNT composite ceramics as a function of PMNT content.

Figure 5.21 presents the plots of T_B and T_{VF} as a function of PMNT content of the BCZT-*0.02*Bi-*x*PMNT composite ceramics. The results showed that the higher temperature than 250°C is a paraelectric state for all sample. When the temperatures were decreased at lower than 250°C is an ergodic relaxor state (ER state). However, the different materials had the different the ER states because the several of chemical compositions led to

different size of PNRs [38]. The temperatures showed lower than 150°C, all materials showed the glassy state which frozen of large PNRs.

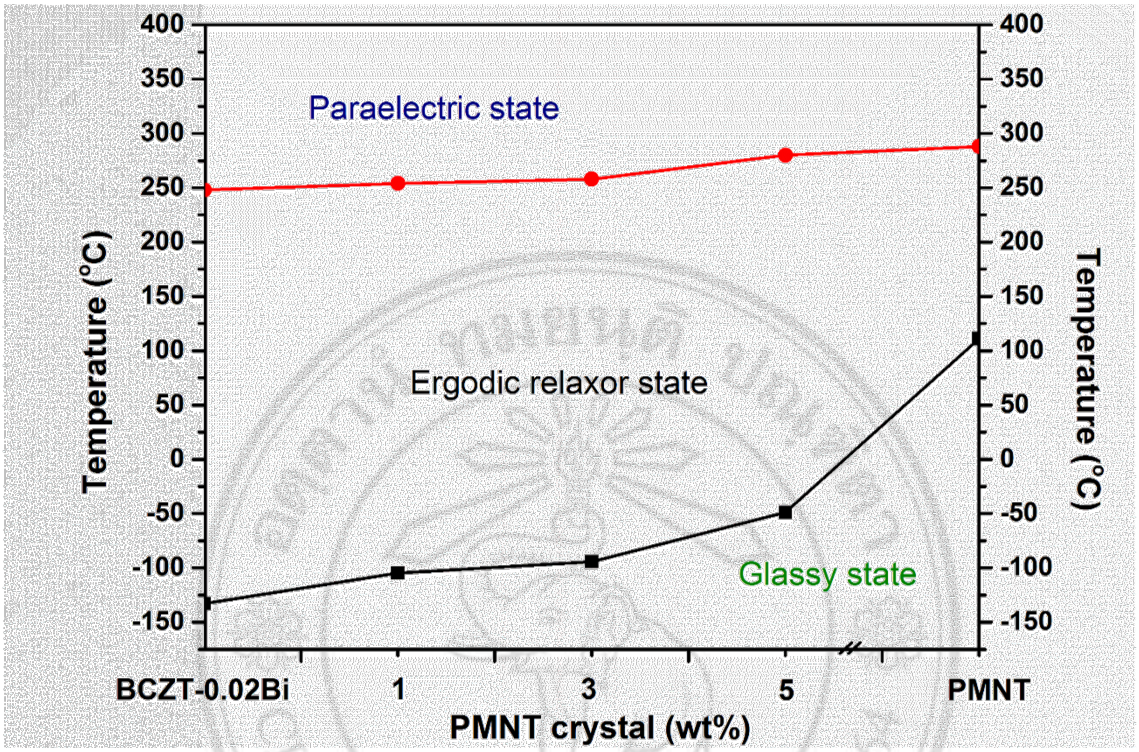

Figure 5.21 Plots of T_B and T_{VF} as a function of PMNT content of the BCZT-*0.02*Bi-*x*PMNT composite ceramics. A temperature range above T_B (red-line) is belonged to a paraelectric state while lower temperature than T_B is presented an ergodic relaxor state. The lower than T_{VF} (black-line) is presented a glassy state.

5.10 Ferroelectric properties of BCZT-*0.02*Bi-*x*PMNT

The observed temperature dependence of P-E loops for BCZT-*0.02*Bi-*x*PMNT ceramics at temperatures 25°C, 0°C, -50°C and -100°C are shown in Figure 5.22 (a)-(d). At 25°C (see Fig. 5.22 (a)), all samples showed linear behavior with very small or no hysteresis. With addition of PMNT crystals, the P-E loop showed a higher slope indicating higher polarizability in the PMNT-embedded samples. At 0°C (Fig. 5.22 (b)) and -50°C (Fig. 5.22 (c)), the P-E loops of PMNT-embedded samples tended to group together and showed similar polarization with small open-up hysteresis regardless of composition. In contrast, the BCZT-*0.02*Bi sample still showed linear, non-hysteretic behavior. This

difference may be related to the value of T_m of each sample: the 0 and -50°C measurement temperatures were close to or below the T_m of 1PMNT and 3PMNT samples but still higher than the T_m of BCZT-*0.02*Bi. Hence, the behavior of dipoles in response to electric field was expected to be different between these samples. The maximum polarization (P_m) of the samples was in the range of 1.57-3.03 μC/cm^2. It might be possible to completely switch the polarization of PMNT crystals [17] by the applied fields but many randomly-oriented grains in BCZT-*0.02*Bi may require higher switching field to obtain similar polarization magnitude. Thus, 1PMNT and 3PMNT ceramic composites exhibited higher P_m values than that of the BCZT-*0.02*Bi ceramic. At -100°C, the P-E loops of all the samples exhibited appreciable hysteretic behavior. It should be noted that this temperature was lower than the T_m of all the samples. Some energy loss may occur due to the sluggish switching of PNRs and upon decreasing applied field, some portions of PNRs may retain some polarization, giving rise to the observed open-up loops. The shift of the freezing temperature (T_{VF}) and the increase in the size and number of PNRs [1] due to the effect of local fields produced by PMNT single crystal may also play a role in the larger hysteresis loop compared to the BCZT-*0.02*Bi ceramic. Nevertheless, the grouping of PMNT-embedded samples clearly showed different ferroelectric behavior from that of BCZT-0.02Bi. The increasing trend of the P_m was obtained with PMNT addition from 1.88 μC/cm^2 (BCZT-*0.02*Bi), to 2.99 μC/cm^2 (1PMNT) and to 3.28 μC/cm^2 (3 PMNT), respectively.

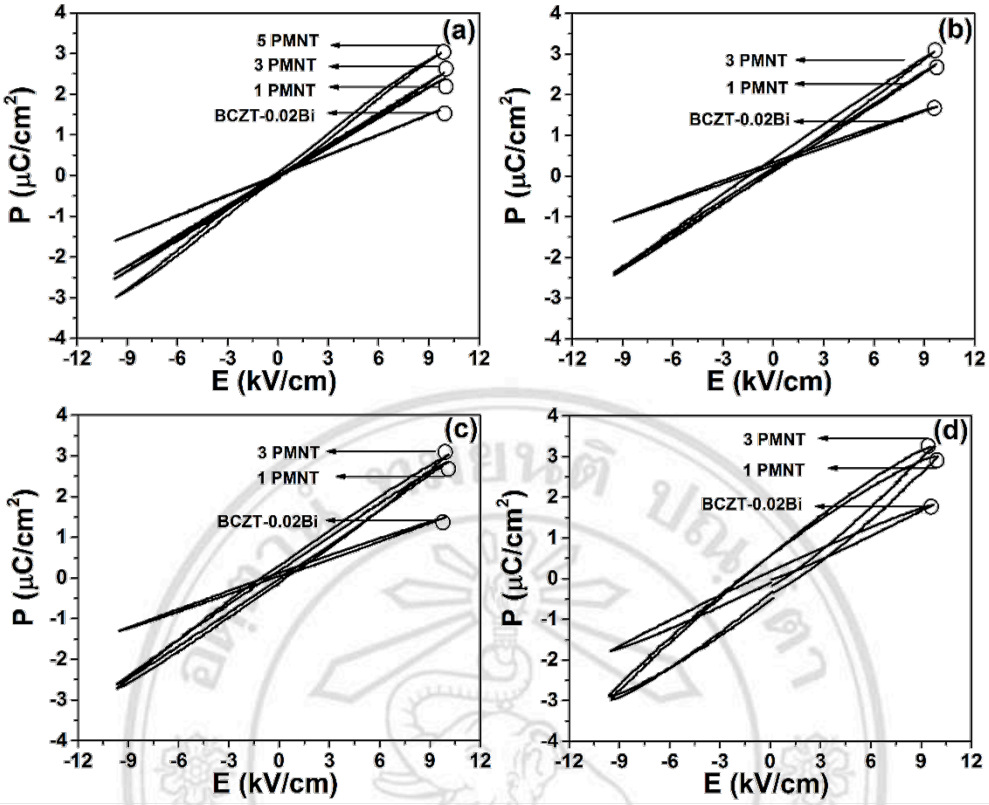

Figure 5.22 P-E loops of BCZT-*0.02*Bi-*x*PMNT displayed at difference temperatures: (a) 25°C, (b) 0°C, (c) -50°C, and (d) -100°C.